Check for updates

small methods
www.small-methods.com

Polyoxometalate Ionic Sponge Enabled Dendrite-Free and Highly Stable Lithium Metal Anode

Yuan Zhong, Yaqing Su, Peng Huang, Qiu Jiang, Yue Lin, Haiyang Wu, Emiel J. M. Hensen, Amr. M. Abdelkader, Kai Xi,* Chao Lai, and Shulei Chou**

Metallic lithium batteries are holding great promises for revolutionizing the current energy storage technologies. However, the formation of dendrite-like morphology of lithium deposition caused by uneven distribution of Li^+ might cause severe safety concerns of batteries. In this study, a polyoxometalate (POM) cluster, $H_5PMo_{10}V_2O_{40}$ ($PMo_{10}V_2$), is added to the conventional electrolyte that can construct a lithium-rich layer and inhibit the growth of Li dendrites effectively. The Li-rich layer can fill any lack of lithium ions on the surface of the metal anode, making the electric field strength consistent across the anode surface, thereby inhibiting the formation of lithium dendrites. Consequently, a significantly prolonged cyclic lifespan is obtained for both Li/Li symmetric cells and Li/$LiCoO_2$ (Li/LCO) full cells. The cells with LCO positive maintains a high reversible specific capacity of 108.5 mAh g^{-1} after 300 cycles when electrolyte with $PMo_{10}V_2$ additive is used, compared to 31.5 mAh g^{-1} for the untreated electrolyte. The findings indicate that POMs endowed as "ionic sponge" can be widely deployed in lithium metal batteries.

1. Introduction

Metallic lithium is considered as one of the most appealing anode materials for the upcoming high-energy and high-power batteries credited to its higher theoretical specific capacity and lowest redox potential. It has widely been applied to constructing high energy density batteries such as Li—O_2 and Li—S batteries.[1,2] Some of the lithium metal batteries (LMBs) start to penetrate the market in some niche applications, such as Bolloré Bluecar battery (solid-state Li/polymer/$LiFePO_4$), OXIS Energy battery (Li—S), and the QinetiQ battery in the Zephyr unmanned aerial vehicle (Li—S). Nevertheless, the large-scale applications of batteries that use Li anode remain challenging for several reasons. The large volume change during repeated Li plating/stripping cycle is a source of mechanical and interfacial instability.[3–6] Also, the unstable solid electrolyte interphase (SEI) layers on the Li surface lead to severe electrolyte decomposition due to the continuous side reactions with the anode. Moreover, lithium's uneven electrodeposition leads to the formation of dendrites, which reduces the Coulombic/energy efficiency and induces safety issues owing to the short-circuiting.[7–9] Several models were developed to explain the source of uncontrolled dendrites growth. The most common model correlates the dendrites formation to the Li anode's surface defects that causes plenty of charge accumulation. The localized electric fields work as the nucleation sits and attract Li-ions from the electrolyte, making them crowding on the sharp tips. As a result, Li grows faster on the nuclei's protruding tips than on the other areas of the anode forming needles-like dendrites.[10–13]

Y. Zhong, P. Huang, H. Wu, C. Lai
School of Chemistry and Materials Science
Jiangsu Normal University
Xuzhou, Jiangsu 221116, China
E-mail: huangpeng@jsnu.edu.cn

Y. Su
School of Chemistry
Xi'an Key Laboratory of Sustainable Energy Materials Chemistry
State Key Laboratory of Electrical Insulation and Power Equipment
Xi'an Jiaotong University
Xi'an 710049, China

Y. Su, E. J. M. Hensen
Laboratory of Inorganic Materials and Catalysis
Schuit Institute of Catalysis
Eindhoven University of Technology
MB Eindhoven 5600, The Netherlands

The ORCID identification number(s) for the author(s) of this article can be found under https://doi.org/10.1002/smtd.202101613.

DOI: 10.1002/smtd.202101613

Q. Jiang, K. Xi
Department of Materials Science and Metallurgy
University of Cambridge
Cambridge CB3 0FS, UK
E-mail: kx210@cam.ac.uk

Y. Lin
Cavendish Laboratory
University of Cambridge
Cambridge CB3 0HE, UK

A. M. Abdelkader
Faculty of Science and Technology
Bournemouth University
Talbot Campus
Fern Barrow
Poole BH12 5BB, UK

S. Chou
Institute for Carbon Neutralization
College of Chemistry and Materials Engineering
Wenzhou University
Wenzhou, Zhejiang 325035, P. R. China
E-mail: chou@wzu.edu.cn

 © 2022 Wiley-VCH GmbH

Besides the effort to understand the challenges' sources, researchers have also tried to introduce some solutions to bring LMBs closer to commercialization. Some of the newly developed solutions include: adding electrolyte additives to tailor its decomposition,[14,15] employing solid-state electrolytes,[16,17] designing an artificial interface layer,[18,19] engineering 3D Li-hosting scaffolds with high conductivity,[20,21] using pulsed currents in the stripping/plating cycles,[22,23] and some other strategy.[24,25] Amongst them, the incorporation of electrolyte additives has shown promising results on improving the anode performance since it can influence the characteristics of SEI directly and change Li^+ electrodeposition behavior. The electrolyte additives can be broadly classified into two types; additives that decompose on the surface, and the additives that can be adsorbed on the surface. Both types form protective coatings on the surface and endorse the stability of the SEI. Examples of the decomposing additives include vinylene carbonate and fluoroethylene carbonate. Caesium ions, cationic surfactants, and ionic liquids are amongst the adsorbed additives investigated in the literature.[26–31] Although various additives have been reported, looking for new electrolyte additives to improving the uniformity of Li-ion distribution and constructing stable SEI film on the surface of the anode still needs further investigation.

Polyoxometalates (POMs), as a significant class of transition metal-oxo cluster, could be promising candidates due to their stable structures, uniform size, reversible multielectron redox properties, and ability to mediate redox reaction in a couple of systems. Concerning lithium batteries, POMs have been utilized as the positive electrode material in lithium-ion batteries. The multielectron redox capability provides good capacities, especially the Keggin-based POM structures. The POM with a Keggin structure can absorb great amount of Li^+ and exhibit the characteristics of an "ionic sponge" (Figure S1, Supporting Information).[32–34] We also predict that applying it into the lithium metal batteries can build a stable SEI film and regulate uniform lithium deposition during plating and stripping.

In this work, we report a polyoxometalate material $H_5PMo_{10}V_2O_{40}$ (denoted as $PMo_{10}V_2$) as an effective electrolyte additive to ease the continuous growth of lithium dendrites. The $\{PMo_{10}V_2O_{40}\}^{x-}$ (x = 5–20) complex worked as "ionic sponge" that can absorb a large number of Li^+, making them lithium-rich. As shown in **Figure 1**a, the $PMo_{10}V_2$ additives coordinate with Li^+ to form Li-rich interfacial layer in which the ionic sponge structure can fill the lack of Li^+ on the surface of metal anode. This regulates the electric field strengths across the anode surface and thereby inhibiting the formation of lithium dendrites. Also, the $PMo_{10}V_2$ additives render the construction of a rigid and stable SEI layer that reduces the successive decomposition of the electrolyte. Finally, the electrolyte additive of $PMo_{10}V_2$ enhances the capability of cycling in Li/Li symmetric cells and Li/$LiCoO_2$ (Li/LCO) full cells, delivering a higher reversible specific capacity of 108.5 mAh g^{-1} after 300 cycles compared to that of the blank electrolyte (31.5 mAh g^{-1}).

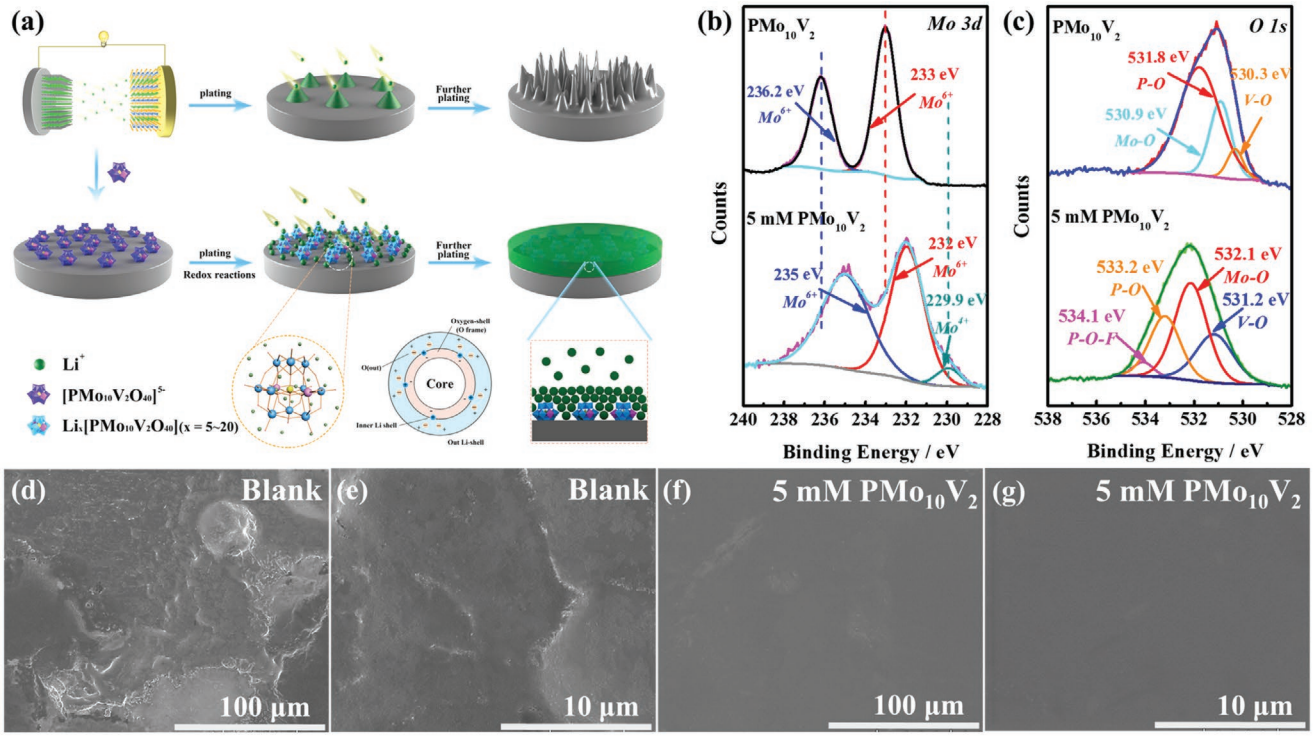

Figure 1. a) Diagram of lithium deposition with $PMo_{10}V_2$ additive or untreated electrolyte. XPS spectra of Li anode using $PMo_{10}V_2$ additive or untreated electrolyte. The spectra of b) Mo 3d and c) O 1s of the lithium anode with $PMo_{10}V_2$ additive or untreated electrolyte after soaking in electrolyte for 24 h. Top-view SEM images of lithium soaking in electrolyte for 24 h d,e) with untreated electrolyte and f,g) with $PMo_{10}V_2$ additive.

© 2022 Wiley-VCH GmbH

2. Results and Discussion

The composition of this layer can be determined using X-ray photoelectron spectroscopy (XPS) for the surface of the Li foil after immersed in the electrolyte for 24 h. Although detecting lithium with XPS is a challenge, there are many pieces of evidence that this layer is a result of the reaction between lithium and $PMo_{10}V_2$. The high-resolution Mo 3d spectrum shows a signal of Mo^{4+} at 229.9 eV, indicating the Mo^{6+} in $PMo_{10}V_2$ is reduced to Mo^{4+} (Figure 1b). Also, a signal of P—O—F can be observed in the O1s spectrum at ≈534.1 eV after adding $PMo_{10}V_2$ to the electrolyte (Figure 1c).[35,36] Meanwhile, the surface morphology of the Li foil immersed in the electrolyte for 24 h is obtained using a scanning electron microscope (SEM). Compared with the anode where the untreated electrolyte is used (Figure 1d,e), the lithium foil's surface is flatter and smoother when $PMo_{10}V_2$ was added (Figure 1f,g). The adsorbed layer is also evidenced by the energy dispersive spectroscopy (EDS) element analysis for the lithium foil soaked in the electrolyte containing the $PMo_{10}V_2$ additive for 24 h (Figure S2, Supporting Information). To further verify the adsorption of $PMo_{10}V_2$ on the lithium surface, differential capacitance–potential curves were recorded with and without additive (Figure S3, Supporting Information). The capacitance is significantly lower when $PMo_{10}V_2$ was added to the electrolyte. Also, the unmodified electrolyte's capacitance has bell-like shaped nearly without potential independent regions, reflecting changes in specific adsorption at that surface. The curve is flattened after adding $PMo_{10}V_2$ to the electrolyte, with adsorption peak at ≈ –0.52 V, indicating the additive is firmly adsorbed on the Li surface. Furthermore, the contact angle measurement on the Li surface shows a significant decrease from 28.5° for the blank electrolyte to 18.7° for the treated electrolyte (Figure S4, Supporting Information). Furthermore, Zeta potential measurements recorded higher value at the electrode/electrolyte interface when $PMo_{10}V_2$ was added to the electrolyte (Figure S5, Supporting Information). This is contributed to the formation of a more stable surface layer comprising of $PMo_{10}V_2$. These results prove that $PMo_{10}V_2$ adsorbed well on the Li surface, which enhances the wettability of the electrode.[37,38] Therefore, the electrolyte additive is expected to play roles in protecting the electrode and facilitating the interaction at the interface.

So as to explore the role of $PMo_{10}V_2$ electrolyte additive on the surface of lithium metal anodes, the evolution of Li deposits was monitored via an in situ optical microscopy. As evidenced in Figure S6 in the Supporting Information, without $PMo_{10}V_2$ additive, some protuberances start to come out of the surface after electroplating for 1 min at a high current density of 4.0 mA cm^{-2}. In less than 5 min, obvious dendrites can be monitored and the Li anode becomes mossy. For the blank electrolyte, the irreversible Li deposits derived from the uneven Li^+ flux suggest successive consumption of both metallic anode and liquid electrolyte, resulting in low Coulombic efficiencies and specific capacity degradation of the batteries. On the contrary, $PMo_{10}V_2$ additive facilitates the formation of a smooth and flat Li anode surface without any obvious protuberance. In addition, to explore the effect of $PMo_{10}V_2$ additive on Li^+ deposition, Li/Cu batteries were assembled and cycled for three times. Finally, the surface of copper foil was detected by SEM (Figure S7a–d, Supporting Information). Compared with the untreated electrolyte, the Cu electrode in the electrolyte containing $PMo_{10}V_2$ additive shows a smoother morphology. It can also be seen from SEM-mapping that the additives are evenly distributed on the surface of the Cu electrode (Figure S7e–h, Supporting Information), indicating that the additives are involved in the regulation of Li^+ deposition behavior. From the above evidence, it can be seen that the $PMo_{10}V_2$ additive reacts with the surface of the lithium foil to produce a stable, functional molecular layer, and it can effectively improve the surface morphology of the Li/Cu foil and inhibit the growth of Li dendrites during the stripping/plating cycles.

To further demonstrate the Li anode's stability after modifying the electrolyte, the electrochemical performances of symmetric cells were tested and presented in **Figure 2**, including long-term cycling capability, rate performance, and electrochemical impedance spectroscopy (EIS). Symmetric Li|Li cells with $PMo_{10}V_2$ additive maintain a stable operation for 360 h at the current density of 1.0 mA cm^{-2} with a reversible electroplating capacity of 0.5 mAh cm^{-2}. When the applied current density increases to 2.0 mA cm^{-2} (fixed capacity of 1 mAh cm^{-2}), the cells can cycle for 140 h without a short-circuit phenomenon (Figure 2a,b). The voltage profiles of stripping/plating curves were also examined to reveal the advantage of $PMo_{10}V_2$ additive. For the unmodified electrolyte, significant voltage fluctuations can be observed which is followed by sharp deterioration. The voltage polarization enlarges when increasing the number of cycles, indicating the electrodes' instability due to dendrite formation.[39] At a current density of 1.0 mA cm^{-2}, the cell with $PMo_{10}V_2$ additive delivers voltage polarization value of about 75 mV, which adds up to 100 mV at 2.0 mA cm^{-2}. The measured overpotential was significantly higher without additive, resulting in a short circuit after a few cycles. The cells' rate capability with different electrolytes was determined under current densities of 1.0, 2.0, and 4.0 mA cm^{-2} under areal capacities of 0.5, 1.0, and 2.0 mAh cm^{-2}, respectively. The voltage hysteresis of Li anode with $PMo_{10}V_2$ additive is well maintained with values of ≈110.0 mV at 1.0 mA cm^{-2} and ≈210.0 mV at 4.0 mA cm^{-2}, respectively (Figure 2c). On the contrary, the blank electrolyte's voltage hysteresis significantly increases with increasing the current density to 4.0 mA cm^{-2} and could not recover the same voltage value after cycling again at lower current density. To further illustrate Li metal batteries' stability using $PMo_{10}V_2$ additive, we used asymmetrical Li-Cu cells and recorded the voltage-capacity profiles after different cycles with blank and modified electrolytes (Figure S8, Supporting Information). In general, the capacity is higher for the cells with modified electrolyte than with blank electrolyte, indicating the ionic sponge $PMo_{10}V_2$ helps to attract more Li ions to the anode surface.[33] The columbic efficiency, as a good indicator of cell stability, is higher when the electrolyte has $PMo_{10}V_2$ electrolyte additive. Without it, the columbic efficiency significantly reduced with cycling and the capacity after 50 cycles is less than 20% of the value at the end of the second cycle. In addition, we assembled a Li|Li symmetric battery with fixed capacity of 2 and 3 mAh cm^{-2} for long-term cycling and found that electrolytes with additives have better cycle stability and longer cycle life (Figure S9, Supporting Information).

© 2022 Wiley-VCH GmbH

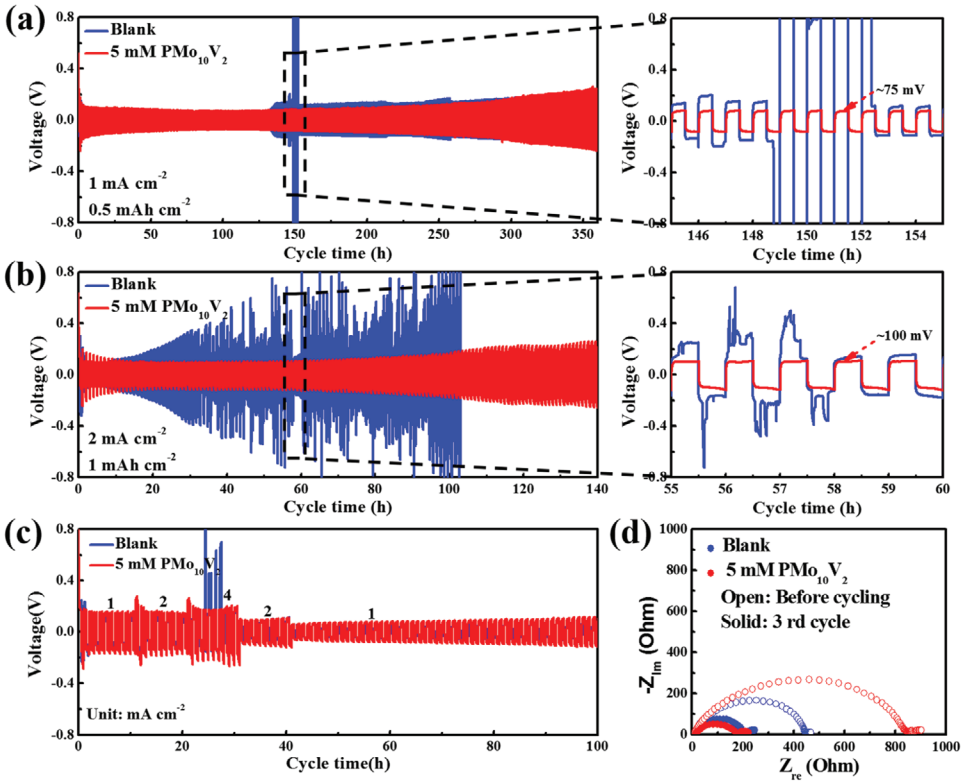

Figure 2. Voltage profiles of Li|Li cells fabricated with $PMo_{10}V_2$ additive or untreated electrolyte, at current densities of a) 1.0 mA cm^{-2} for 0.5 h and b) 2.0 mA cm^{-2} for 0.5 h, respectively. c) Rate capability of Li|Li cells determined at current densities of 1.0, 2.0, and 4.0 mA cm^{-2} for 0.5 h, respectively. d) EIS results of Li|Li cells before cycling and cycling three times at 2.0 mA cm^{-2} for 0.5 h.

Furthermore, we investigated Li|Li symmetrical cells performance with different concentration of $PMo_{10}V_2$ in the electrolyte. The ionic conductivity of the liquid electrolyte increases with the higher concentration of $PMo_{10}V_2$ additive (Figure S10, Supporting Information). The cycling performances of different electrolyte compositions are presented in Figure S11 in the Supporting Information. The surface layer formed on the Li anode after adding $PMo_{10}V_2$ to the electrolyte is not always protective. Compared to the electrolyte with 5×10^{-3} M $PMo_{10}V_2$ additive, inferior cycling performance can be observed for electrolyte with other concentration. For low concentrations of 1.0×10^{-3} and 2×10^{-3} M, it is obvious that the formed layer does not fully cover the Li surface and cannot satisfy a uniform distribution of the charge; hence dendrites can still form. Nevertheless, contrary to our expectations, electrolyte with a higher concentration of additives (8.0×10^{-3} M) is not effective to promote stability to the anode. This is probably because of the formation of a thicker layer on Li anode that a) hinders Li^+ diffusion toward the electrode and b) increases the overall resistance of the electrode.[30]

The charge transfer resistance at a high and medium concentration of $PMo_{10}V_2$ can find further evidence from the EIS measurements. The Nyquist plots obtained from Li|Li symmetric cells with different liquid electrolytes are given (Figure 2d). After fitting, the charge-transfer impedance (R_{ct}) in the high-frequency range of the untreated electrolyte (442.9 Ω) is lower than that of the electrolyte with $PMo_{10}V_2$ additive (812 Ω) before cycling. The increased R_{ct} after cycling can be ascribed to the adsorption of $PMo_{10}V_2$ molecules on the interface. The adsorbed $PMo_{10}V_2$ layer acts as an intermediate to tailor the transportation of Li^+.[40] Interestingly, after the 3rd plating/stripping cycle, the resistance of SEI (R_{SEI}) and R_{ct} with $PMo_{10}V_2$ additive is much smaller than that of the unmodified electrolyte (Table S1, Supporting Information), which is mainly attributed to the construction of the stable solid–liquid interface due to the ionic accumulation effect of $PMo_{10}V_2$. Dendrites formation and the accumulation of resistive substances from the electrolyte decomposition in the cell without $PMo_{10}V_2$ additive are responsible for increasing the cell impedance. Also, it seems that the $PMo_{10}V_2$ layer adsorbed on the electrode can be beneficial to the construction of a stable SEI film.

A similar phenomenon can be seen by observing SEM images of the cycled Li surface at 4.0 mA cm^{-2} under plating deposition of 2 mAh cm^{-2} (**Figure 3**). Metallic Li surface after cycling without $PMo_{10}V_2$ additive shows very porous morphology on the entire electrode with lots of dendrites and cracks (Figure 3a,b). After adding $PMo_{10}V_2$, a dense and smooth surface of Li foil with almost no cracks or imperfection can be maintained after 30 cycles (Figure 3d,e). Moreover, as shown in the cross-sectional SEM image (Figure 3c), more than half of the foil transformed into a grain-like structure with obvious cracks after cycling in the unmodified electrolyte. For the electrolyte with $PMo_{10}V_2$ additive, the lithium foil retained its structures, without any obvious cracks or voids throughout the cross-section (Figure 3f). These results prove that $PMo_{10}V_2$ additive can form a protective layer on Li metal anode that effectively

© 2022 Wiley-VCH GmbH

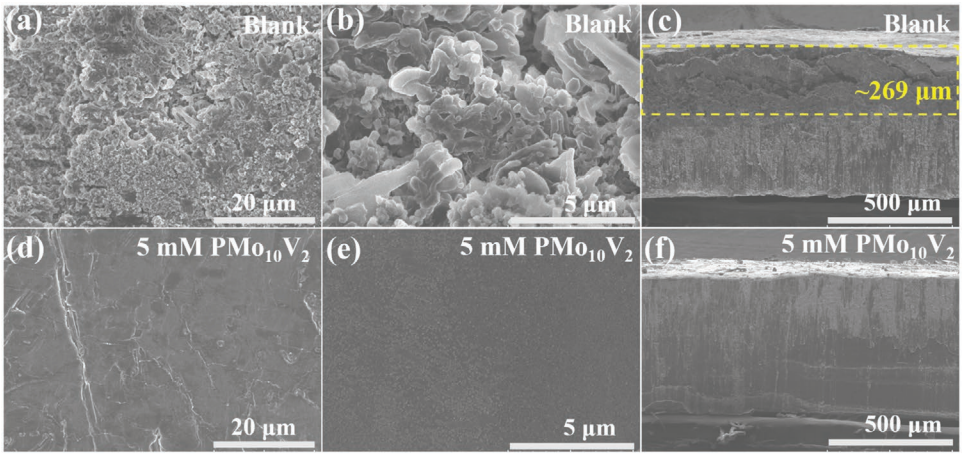

Figure 3. SEM images of Li anodes from a,b,d,e) top-view and c,f) cross-sectional disassembled from the Li||Li symmetric cells using with or without $PMo_{10}V_2$ additive after plating/stripping for 30 cycles at 4.0 mA cm^{-2} (current density) and 2 mAh cm^{-2} (fixed capacity).

suppress dendrite growth and lead to the formation of a stable SEI layer, hence improving the cycle life of lithium batteries.

To verify the $PMo_{10}V_2$-containing SEI film formation stability, XPS analysis was conducted for the lithium anode surface with and without additive after three cycles (**Figure 4**). Similar to the XPS results of the Li foil before charging/discharging, the wide scan confirmed the presence of Mo, P, O, and F when cycling in the presence of $PMo_{10}V_2$. The high-resolution Mo 3d spectrum (Figure 4b) shows a signal of Mo^{4+} at 226.1 eV together with Mo^{6+} peak and satellite at 232.2 and 236.8 eV, respectively.[35] This suggests the SEI layer's composition is somewhat complex and has more than one oxidation state of molybdenum. The O 1s spectrum shows several peaks related to the O—Mo and V—O bonds, as well as that corresponding to the Mo—O bonds after cycling in the electrolyte with additive, further confirming the role of $PMo_{10}V_2$ in forming stable SEI layer (Figure 4c,d).[41] Also, comparing the Fourier transform infrared (FTIR) spectra of the surface layer before and after cycling proves the structure of $PMo_{10}V_2$ is stable on the Li foil (Figure S12, Supporting Information). The electrolyte, however, changed the color from yellow to blue after cycling, indicating a reaction between $PMo_{10}V_2$ and Li ions to form a heteropoly blue compound, with the general formula $Li_x\{PMo_{10}V_2O_{40}\}$ (x = 5–20)) (Figure S13, Supporting Information).[42]

To evaluate the performance of the electrolyte with $PMo_{10}V_2$ additive in practical applications, we tested it in full cells

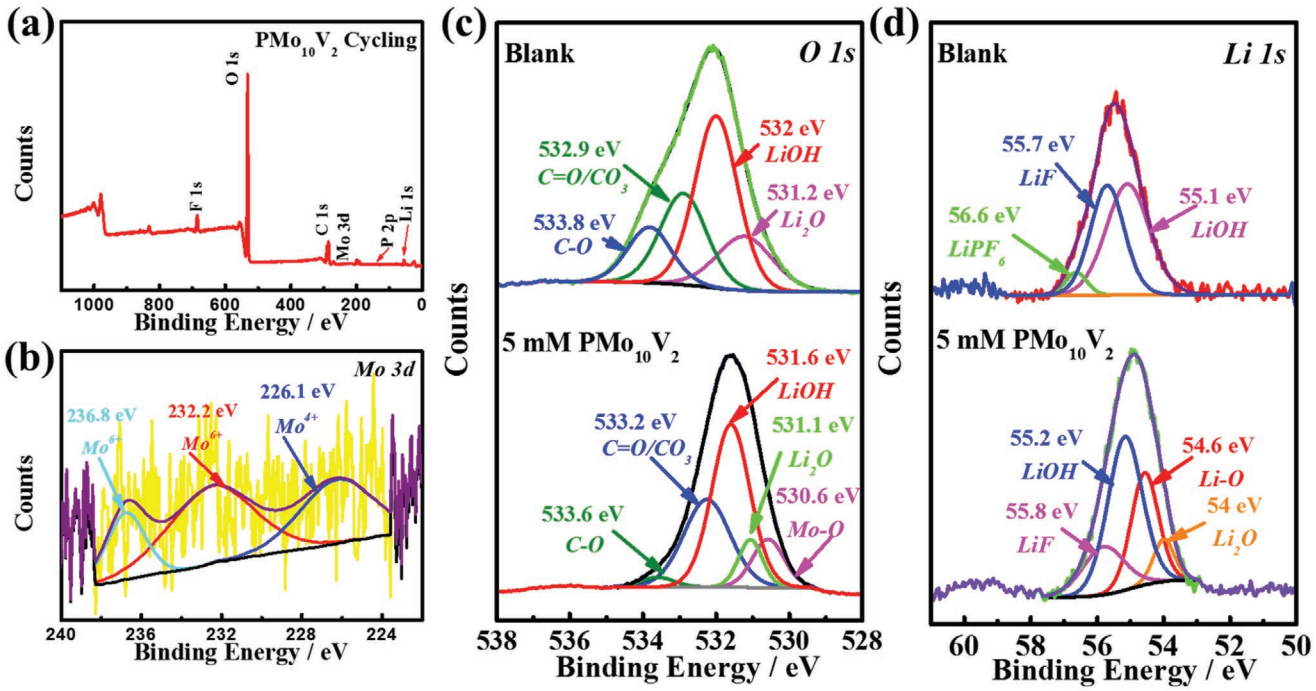

Figure 4. a) XPS wide scan spectra of $PMo_{10}V_2$. b) Mo 3d XPS spectrum. The spectra of c) O 1s and d) Li 1s on the lithium anode's without or with $PMo_{10}V_2$ additive after three cycles.

© 2022 Wiley-VCH GmbH

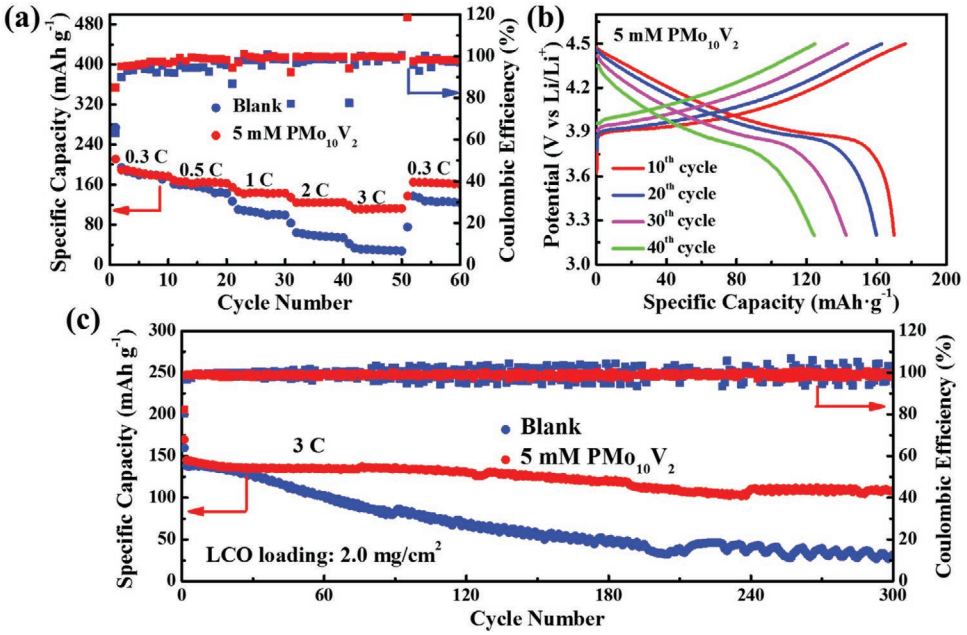

Figure 5. a) Electrochemical capability of Li|$LiCoO_2$ with $PMo_{10}V_2$ additive or untreated electrolyte. b) Voltage profiles of Li|$LiCoO_2$ cells in the electrolyte with $PMo_{10}V_2$ additive. c) Cycling capability of Li|$LiCoO_2$ full cells with $PMo_{10}V_2$ additive or untreated electrolyte at high current rate of 3 C.

using a $LiCoO_2$ cathode. The $PMo_{10}V_2$ additive to the electrolyte helped the cell achieving high rate capability. The cell with $PMo_{10}V_2$ additive can reach reversible capacities of 175, 162.9, and 143.3 mAh g^{-1} at current rates of 0.3, 0.5, and 1 C, respectively (**Figure 5**a). The cell could maintain a high reversible specific capacity of 112.6 mAh g^{-1} at a high rate (3 C). When cycled back at 0.3 C, the cell can recover a capacity of 173 mAh g^{-1}. In contrast, the cell with blank electrolyte has comparable capacity at a low rate (142.5, 99.3, 54.1, and 27.6 mAh g^{-1} at 0.5, 1, 2, and 3 C). Still, the capacity significantly dropped to 27.6 mAh g^{-1} at 3 C (Figure 5b and Figure S14, Supporting Information). Even under high-load LCO cathode conditions, it still has great rate performance and cycling stability (Figure S15, Supporting Information).

Although the cell's initial charge–discharge capacity with untreated electrolyte is slightly higher than that of the cell containing $PMo_{10}V_2$ additive, the cycling stability is significantly enhanced after modifying the electrolyte. The long-term cycling performance at a high rate of 3 C is presented in Figure 5c. The full cell with $PMo_{10}V_2$ additive can deliver a charge capacity of 108.5 mAh g^{-1} after 300 cycles at a high rate. This is the highest cycling stability reported for a full cell with Li metal anode at such high rate to the best of our knowledge. On the other hand, the cell with blank electrolyte suffers capacity fade after only 20 cycles. Compared with different improvement strategies, the batteries using $PMo_{10}V_2$ electrolyte additive have better performance when matching high voltage $LiCoO_2$ cathode material (Table S2, Supporting Information). Thus, the characteristic of "ionic sponge" can promote high rate capability and long cycling and display promising potential in specific energy storage applications.

To elaborate the role of $PMo_{10}V_2$ on Li^+ transport, density functional theory (DFT) calculations were conducted. The charge distributions of Li^+ adsorbed on the surface of $PMo_{10}V_2$, Li <001>, Li <110>, and Li <111> crystal planes were investigated respectively, exhibiting that the combination between $PMo_{10}V_2$ and Li^+ is of ionic properties (**Figure 6**a). In contrast, the interaction between Li^+ ions and lithium crystal planes is designated as metallic nature. We then simulated and compared the binding energies for the different surfaces. The results of Li^+ on $PMo_{10}V_2$, Li <001>, Li <110>, and Li <111> are calculated to be −5.68, −1.66, −1.39, and −1.84 eV, respectively (Figure 6b). The stronger interaction of Li^+ to $PMo_{10}V_2$ molecule than to any of the investigated Li crystal planes indicate that the Li^+ are adsorbed preferentially on $PMo_{10}V_2$. Depending on their diffusion properties, the adsorbed Li^+ ions accumulate and tend to spread out uniformly with no directional or localized growth. Therefore, we further investigated the Li^+ diffusion behavior and Li^+' migratory barriers on various surfaces. These results suggest that the adsorbed Li^+ preferably aggregate on the crystal plane of Li <111> because of the highest diffusion barrier compared with that of Li <001> and Li <110> crystal planes, causing higher concentration at its tips.[43] In contrast, the $PMo_{10}V_2$ has a unique 3D structure with a low migratory barrier (0.12 eV), revealing facile diffusion and uniform distribution of the adsorbed Li^+ on the $PMo_{10}V_2$ surface (Figure 6c). Overall, the transfer mechanism of Li^+ in $PMo_{10}V_2$-doped electrolyte and the following deposition can be depicted in three steps. First, Li^+ forms a complex with $PMo_{10}V_2$, which subsequently leads to a homogeneous distribution of Li^+ on the surface of Li anode. The formation of the Li^+-$PMo_{10}V_2$ complex is supported by the stronger binding between Li^+ and $PMo_{10}V_2$ (−5.68 eV), which is stronger than the binding between Li^+ and metallic Li, ethyl carbonate (EC), dimethyl carbonate (DMC), or ethyl methyl carbonate (EMC). Second, the adsorbed Li ions detach from the surface $PMo_{10}V_2$-containing layer, resulting in slightly elevated overpotential (≈338.2 mV) as shown in Figure 6d. The detached Li^+ then migrate from $PMo_{10}V_2$ to the current collector's surface

© 2022 Wiley-VCH GmbH

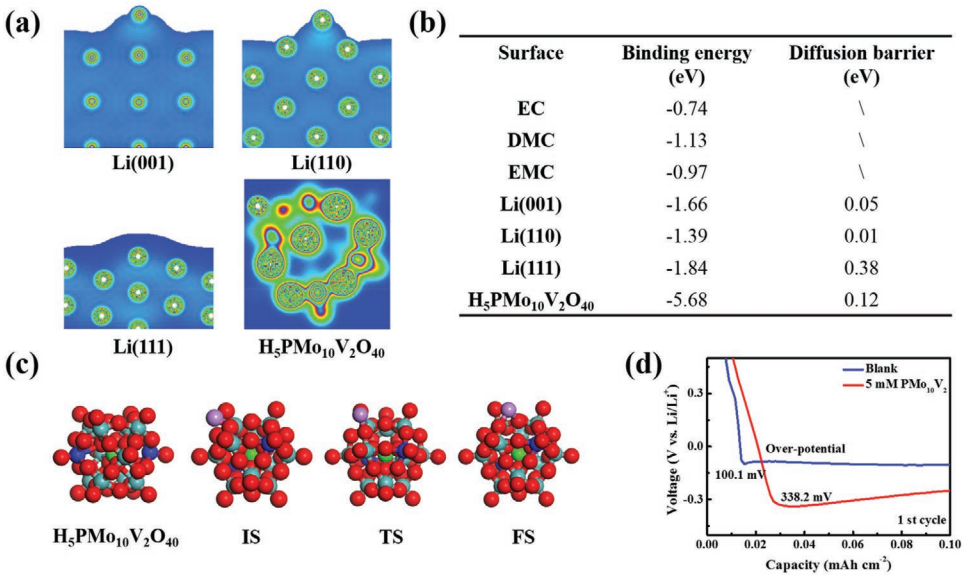

Surface	Binding energy (eV)	Diffusion barrier (eV)
EC	-0.74	\
DMC	-1.13	\
EMC	-0.97	\
Li(001)	-1.66	0.05
Li(110)	-1.39	0.01
Li(111)	-1.84	0.38
$H_5PMo_{10}V_2O_{40}$	-5.68	0.12

Figure 6. a) The distribution of charge of Li^+ on the planes of $PMo_{10}V_2$, Li <001>, Li <110>, and Li <111>, respectively. b) The binding energy and diffusion barrier of Li^+ on the surfaces. c) The behavior of Li^+ migrated on the $PMo_{10}V_2$ surface. d) The voltage hysteresis of symmetric Li|Cu cells using $PMo_{10}V_2$-based or untreated electrolyte.

to produce Li deposits. Finally, because of the strong adhesion between the $PMo_{10}V_2$ layer and the Li anode, the Li deposits can contact and wet the $PMo_{10}V_2$ particles, and then grow along the surface, enabling dendrite-free anodes.

3. Conclusion

In summary, the additive $PMo_{10}V_2$ anion cluster acts as "electron sponge" to attract Li^+ from the electrolyte through electrostatic force, forming a Li^+-rich bundles, which then form an interfacial layer on the Li metal before electrolysis. This layer grew to a thicker and more protective SEI layer on the anode during the initial several cycles. Several spectroscopic and electrochemical techniques proved the stability of the formed layer. The $PMo_{10}V_2$-containing layer also helped to replenish the lithium ions' vacancies on the lithium foil, which homogenized the charge distribution on the surface and subsequently prevented the localized deposition of Li into dendrites. Meanwhile, the DFT calculations shade more clear on such mechanism discussion above. First, Li^+ forms a complex with $PMo_{10}V_2$ clusters due to the high binding energies, and then the Li ions get detached from the $PMo_{10}V_2$-containing layer and diffuse toward the anode. Due to the low migration barriers for Li on the $PMo_{10}V_2$-containing layer, the distribution of the deposited lithium is homogeneous across the anode surface. As a result, the Li anodes in the carbonate electrolyte with $PMo_{10}V_2$ ionic sponge additive exhibited an excellent cycle stability for 360 h at a current density of 1 mA cm^{-2}, and outstanding rate performance up to 2 mA cm^{-2}. When added $PMo_{10}V_2$ to the electrolyte in a full Li-$LiCoO_2$ cell, excellent cyclic stability and rate capability were obtained. The cell was able to deliver a high reversible capacity of 108.5 mAh g^{-1} at 3 C up to 300 cycles. Our work presented an efficient mechanism for suppressing dendritic growth on lithium metal anodes, provides an effective approach in the form of lithium-rich interface layer, and enables the realization of safe and durable LMBs.

4. Experimental Section

Synthesis of Compound of $H_5PMo_{10}V_2O_{40}$: $NaVO_3$ (0.2 mol) and Na_2HPO_4 (0.05 mol) were dissolved in deionized water (100 mL), respectively. The above solutions were mixed and then concentrated H_2SO_4 (5 mL) was added after the solution was cooled. $Na_2MoO_4{\bullet}2H_2O$ (0.5 mol) dissolving in deionized water (200 mL) was added to above mixture. Concentrated sulfuric acid (85 mL) added to above mixture drop by drop and the temperature of hot mixture solution dropped to room temperature while the solution was vigorously stirred. $H_5PMo_{10}V_2O_{40}$ was extracted with ethyl ether (500 mL). Air was blown into the bottom layer in order to remove ether. The solid was dissolved in small amount of deionized water, then concentrated to form initial crystal, and then crystallized further. The obtained crystals were red after the treatment of filtering, washing with deionized water, and drying in air under room temperature.[44]

Chemicals: $H_5PMo_{10}V_2O_{40}$ ($PMo_{10}V_2$) with a Keggin-type structure (see the inset of Figure 1a) was obtained as described in the previous article and characterized by FTIR spectra and X-ray spectra (Figures S12 and S16, Supporting Information). In the FTIR spectrum, the peaks at 1055–1100, 1000–900 (sharp), and 900–700 cm^{-1} are attributed to P—O, Mo=O, and metal–oxygen–metal bonds, respectively. The V—O absorption may be masked by that of Mo—O. Several other techniques characterized the compound and the obtained consequences are in good consistent with the literature.[45] $LiCoO_2$ was purchased from Shanghai Aladdin Biochemical Technology Co., Ltd. Li foil (>99.99%) with a diameter of 14 mm and thickness of 600 µm was purchased from China Energy Lithium Co., Ltd.

Electrochemical Measurements: All the cells were assembled in an argon-filled glovebox. To explore the electrochemical performance of the $PMo_{10}V_2$ electrolyte additive, symmetrical Li|Li cells were first assembled in coin cells (CR2032 type) using Celgard 2300 separators and Li foil electrodes at room temperature. The untreated electrolyte was $LiPF_6$ (1.0 M) dissolved in a mixture (EC/DMC/EMC = 1/1/1). The as-prepared $PMo_{10}V_2$ was added to the electrolyte with the target concentration (1×10^{-3}, 2×10^{-3}, 3×10^{-3}, 5×10^{-3}, and 8×10^{-3} M). Symmetric cells with 30 µL of

© 2022 Wiley-VCH GmbH

electrolyte were galvanostatic cycled under current densities of 1.0 and 2.0 mA cm^{-2}. The Li/LCO full cells were assembled with LCO cathodes, Li foil anodes, and Celgard 2300 separators in a CR2032 type coin cell. For the preparation of LCO cathodes, the mixture slurry of LCO, Super P conductive carbon, and polyvinylidene fluoride in a mass ratio of 7:2:1 was coated on Al foil with the dispersed solvent of 1-methyl-2-pyrrolidinone, then dried at 60 °C for 12 h in a vacuum oven, and finally punched into a piece of electrode with 10 mm diameter. The mass loading of the LCO cathode is ≈1.0 mg cm^{-2}. The galvanostatic tests of full cells were conducted within a voltage range from 3.2 to 4.5 V at rates of 0.3, 0.5, 1, 2, and 3 C (1 C = 274 mAh g^{-1}). The performance of charge/discharge tests were performed on a battery testing system (LAND, CT2001A). Electrochemical impedance spectra (EIS) were collected under frequency range from 10 mHz to 100 kHz with an amplitude of 5 mV (Chenhua, CHI760E). Differential capacitance curves were carried out by impedance methods within a voltage range from –0.6 to 0.6 V (Solartron 1287). The testing frequency was 1 kHz with amplitude signal of 5 mV. The sweep rate of differential capacitance is 10 mV s^{-1}. The following equation was used to calculate the capacitance

$$C = (2\pi fZim)^{-1} \quad (1)$$

where C is the capacitance, f is the frequency of alternating current perturbation, and Zim is the imaginary component of the impedance.

Computational Methods: All results were figured out as implemented in the Vienna ab initio simulation package in the framework of the spin-polarized DFT. The ion-electron reciprocities are delivered by the projector-augmented wave method and the electron exchange-correlation by the generalized gradient approximation. The Perdew–Burke–Ernzerhof exchange-correlation functional was adopted and the Kohn–Sham valence states were expanded in a plane-wave basis set with cutoff energy of 400 eV. The Li (2s, 2p), O (2s, 2p), V (3d, 4s), Mo (4d, 5s), and P (3s, 3p) electrons were treated as valence states. The optimized lattice constant of Li bulk is 3.49 Å. For Brillouin zone integration, the 7 × 7 × 1 Monkhorst–Pack mesh was used with a vacuum gap of 15 Å. The climbing image nudged-elastic band algorithm was used to mimic the diffusion behavior of Li ions. The total energy difference was less than 10^{-4} eV and the relaxation convergence criterion was set at 0.02 eV $Å^{-1}$.[46–50]

Materials Characterization: The morphological changes and energy dispersive spectrum (EDS) of the Li anodes in symmetric cells before and after cycling were tested by SEM (Hitachi SU8010). The in situ observations of morphology evolution were detected by an optical microscopy (Nikon SMZ1270). Contact angles of different electrolytes on lithium metal and separator were detected by a Dataphysics OCA20 instrument. The Zeta potentials of electrolyte were measured by an automatic measuring instrument ((Malvern) Zetasizer Nano S90).

Supporting Information

Supporting Information is available from the Wiley Online Library or from the author.

Acknowledgements

This work was financially supported by the National Natural Science Foundation of China (No. 51871113) and Natural Science Foundation of Jiangsu Province (BK20200047). Y.S. acknowledges the "Young Talent Support Plan" of Xi'an Jiaotong University. Supercomputing facilities were supported by Hefei Advanced Computing Center and the Netherlands Organization for Scientific Research (NWO).

Conflict of Interest

The authors declare no conflict of interest.

Authors Contribution

P.H., C.L., K.X., and S.C. conceived and designed the research. Y.Z. performed the preparation of material and electrode, the fabrication, and measurement of device. Y.S. and E.J.M.H. performed theoretical simulations. P.H., C.L., and Y.Z. participated in the result discussion and data analysis. P.H., C.L., Y.Z., K.X., and S.C. wrote the paper. All authors read, commented on, and revised the paper. C.L., P.H., K.X., and S.C. supervised the project.

Data Availability Statement

The data that support the findings of this study are available from the corresponding author upon reasonable request.

Keywords

electrolyte additives, ionic sponge, lithium metal anodes, polyoxometalates

Received: December 27, 2021
Published online:

[1] H. Kim, G. Jeong, Y. Kim, J. Kim, C. Park, H. Sohn, *Chem. Soc. Rev.* **2013**, *42*, 9011.
[2] Y. Guo, H. Li, T. Zhai, *Adv. Mater.* **2017**, *29*, 1700007.
[3] H. Zhang, G. Eshetu, X. Judez, C. Li, L. Rodriguez-Martinez, M. Armand, *Angew. Chem., Int. Ed.* **2018**, *57*, 15002.
[4] D. Lin, Y. Liu, Y. Cui, *Nat. Nanotechnol.* **2017**, *12*, 194.
[5] W. Xu, J. Wang, F. Ding, X. Chen, E. Nasybutin, Y. Zhang, J. Zhang, *Energy Environ. Sci.* **2014**, *7*, 513.
[6] Q. Yun, Y. He, W. Lv, Y. Zhao, B. Li, F. Kang, Q. Yang, *Adv. Mater.* **2016**, *28*, 6932.
[7] X. Cheng, R. Zhang, C. Zhao, F. Wei, J. Zhang, Q. Zhang, *Adv. Sci.* **2016**, *3*, 1500213.
[8] N. Li, Y. Yin, J. Li, C. Zhang, Y. Guo, *Adv. Sci.* **2017**, *4*, 1600400.
[9] X. Shen, H. Liu, X. Cheng, C. Yan, J. Huang, *Energy Storage Mater.* **2018**, *12*, 161.
[10] A. Zhamu, G. Chen, C. Liu, D. Neff, Q. Fang, Z. Yu, W. Xiong, Y. Wang, X. Wang, B. Jang, *Energy Environ. Sci.* **2012**, *5*, 5701.
[11] L. Li, S. Li, Y. Lu, *Chem. Commun.* **2018**, *54*, 6648.
[12] X. Xu, S. Wang, H. Wang, C. Hu, Y. Jin, J. Liu, H. Yan, *J. Energy Chem.* **2018**, *27*, 513.
[13] J. Qian, W. Henderson, W. Xu, P. Bhattacharya, M. Engelhard, O. Borodin, J. Zhang, *Nat. Commun.* **2015**, *6*, 6362.
[14] X. Li, J. Zheng, X. Ren, M. Engelhard, W. Zhao, Q. Li, J. Zhang, W. Xu, *Adv. Energy Mater.* **2018**, *8*, 1703022.
[15] L. Xiao, Z. Zeng, X. Liu, Y. Fang, X. Jiang, Y. Shao, L. Zhuang, X. Ai, H. Yang, Y. Cao, J. Liu, *ACS Energy Lett.* **2019**, *4*, 483.
[16] C. Sun, J. Liu, Y. Gong, D. Wilkinson, J. Zhang, *Nano Energy* **2017**, *33*, 363.
[17] C. Wang, Y. Zhao, Q. Sun, X. Li, Y. Liu, J. Liang, X. Li, X. Lin, R. Li, K. Adair, L. Zhang, R. Yang, S. Lu, X. Sun, *Nano Energy* **2018**, *53*, 168.
[18] C. Yan, X. Cheng, Y. Tian, X. Chen, X. Zhang, W. Li, J. Huang, Q. Zhang, *Adv. Mater.* **2018**, *30*, 1707629.
[19] R. Xu, X. Zhang, X. Cheng, H. Peng, C. Zhao, C. Yan, J. Huang, *Adv. Funct. Mater.* **2018**, *28*, 1705838.
[20] Y. Cheng, X. Ke, Y. Chen, X. Huang, Z. Shi, Z. Guo, *Nano Energy* **2019**, *63*, 103854.
[21] Z. Zheng, Q. Su, Q. Zhang, X. Hu, Y. Yin, R. Wen, H. Ye, Z. Wang, Y. Guo, *Nano Energy* **2019**, *64*, 103910.

 © 2022 Wiley-VCH GmbH

[22] A. Mukhopadhyay, M. Jangid, *Science* **2018**, *359*, 1463.
[23] D. Rehnlund, C. Ihrfors, J. Maibach, L. Nyholm, *Mater. Today* **2018**, *21*, 1010.
[24] C. Li, S. Liu, C. Shi, G. Liang, Z. Lu, R. Fu, D. Wu, *Nat. Commun.* **2019**, *10*, 1363.
[25] M. Ye, Y. Xiao, Z. Cheng, L. Cui, L. Jiang, L. Qu, *Nano Energy* **2018**, *49*, 403.
[26] H. Chen, A. Pei, D. Lin, J. Xie, A. Yang, J. Xu, K. Lin, J. Wang, H. Wang, F. Shi, D. Boyle, Y. Cui, *Adv. Energy Mater.* **2019**, *9*, 1900858.
[27] Z. Hu, S. Zhang, S. Dong, Q. Li, G. Cui, L. Chen, *Chem. Mater.* **2018**, *30*, 4039.
[28] X. Zhang, X. Cheng, X. Chen, C. Yan, Q. Zhang, *Adv. Funct. Mater.* **2017**, *27*, 1605989.
[29] F. Ding, W. Xu, G. Graff, J. Zhang, M. Sushko, X. Chen, Y. Shao, M. Engelhard, Z. Nie, J. Xiao, X. Liu, P. Sushko, J. Liu, J. Zhang, *J. Am. Chem. Soc.* **2013**, *135*, 4450.
[30] H. Dai, K. Xi, X. Liu, C. Lai, S. Zhang, *J. Am. Chem. Soc.* **2018**, *140*, 17515.
[31] Y. Lu, S. Das, S. Moganty, L. Archer, *Adv. Mater.* **2012**, *24*, 4430.
[32] a) D. Long, R. Tsunashima, L. Cronin, L. Archer, *Angew. Chem., Int. Ed.* **2010**, *49*, 1736; b) D. Long, E. Burkholder, L. Cronin, *Chem. Soc. Rev.* **2007**, *36*, 105; c) C. Hill, *Chem. Rev.* **1998**, *98*, 1; d) K. Binnemans, *Chem. Rev.* **2009**, *109*, 4283; e) I. Kozhevnikov, *Chem. Rev.* **1998**, *98*, 171; f) J. Compain, P. Mialane, A. Dolbecq, I. Mbomekalle, J. Marrot, F. Secheresse, E. Riviere, G. Rogez, W. Wernsdorfer, *Angew. Chem., Int. Ed.* **2009**, *48*, 3077; g) C. Fleming, D. Long, N. Mcmillan, J. Johnston, N. Bovet, V. Dhanak, N. Gadegaard, P. Kogerler, L. Cronin, M. Kadodwala, *Nat. Nanotechnol.* **2008**, *3*, 229.
[33] H. Wang, S. Hamanaka, Y. Nishimoto, S. Irle, T. Yokoyama, H. Yoshikawa, K. Awaga, *J. Am. Chem. Soc.* **2012**, *134*, 4918.
[34] Y. Song, R. Tsunashima, *Chem. Soc. Rev.* **2012**, *41*, 7384.
[35] T. Wei, M. Zhang, P. Wu, Y. Tang, S. Li, F. Shen, X. Wang, X. Zhou, Y. Lan, *Nano. Energy* **2017**, *34*, 205.
[36] Y. Wang, Q. Zhang, Z. Xue, L. Yang, J. Wang, F. Meng, Q. Li, H. Pan, J. Zhang, Z. Jiang, W. Yang, X. Yu, L. Gu, H. Li, *Adv. Energy Mater.* **2020**, *10*, 2001413.
[37] V. Lockett, R. Sedev, J. Ralston, M. Horne, T. Rodopoulos, *J. Phys. Chem. C* **2008**, *112*, 7486.
[38] J. Hwang, H. Kim, Y. Sun, *J. Electrochem. Soc.* **2018**, *165*, A5006.
[39] P. Zou, Y. Wang, S. Chiang, X. Wang, F. Kang, C. Yang, *Nat. Commun.* **2018**, *9*, 464.
[40] X. Gu, Y. Wang, C. Lai, J. Qiu, S. Li, Y. Hou, W. Martens, N. Mahmood, S. Zhang, *Nano Res.* **2015**, *8*, 129.
[41] M. Priyadarshini, S. Shanmugan, K. Kirubakaran, A. Thomas, M. Prakash, C. Senthil, C. Lee, K. Vediappan, *J. Phys. Chem. Solids* **2020**, *142*, 109468.
[42] S. Li, Y. Zhou, N. Ma, J. Zhang, Z. Zheng, C. Streb, X. Chen, *Angew. Chem., Int. Ed.* **2020**, *22*, 8537.
[43] Y. Li, Y. Li, A. Pei, K. Yan, Y. Sun, C. Wu, L. Joubert, R. Chin, A. Koh, Y. Yu, J. Perrino, B. Butz, S. Chu, Y. Cui, *Science* **2017**, *358*, 506.
[44] G. Tsigdinos, C. Hallada, *Inorg. Chem.* **1968**, *7*, 437.
[45] P. Zhao, Y. Leng, M. Zhang, J. Wang, Y. Wu, J. Huang, *Chem. Commun.* **2012**, *48*, 5721.
[46] G. Kresse, J. Hafner, *Phys. Rev. B* **1994**, *49*, 14251.
[47] P. Blochl, *Phys. Rev. B* **1994**, *50*, 17953.
[48] J. Perdew, K. Burke, M. Ernzerhof, *Phys. Rev. Lett.* **1996**, *77*, 3865.
[49] G. Henkelman, H. Jonsson, *J. Chem. Phys.* **2000**, *113*, 9978.
[50] D. Sheppard, R. Terrell, G. Henkelman, *J. Chem. Phys.* **2008**, *128*, 134106.

© 2022 Wiley-VCH GmbH